

# IDMS: Instance Depth for Multi-scale Monocular 3D Object Detection

Chao Hu\*  
Liqiang Zhu  
Weibing Qiu  
Weijie Wu

*AI Lab*

*Unicom (Shanghai) Industry Internet Co., Ltd.  
Shanghai, 200000, CHINA*

HUCHAO.000@GMAIL.COM  
ZHULQ0@GMAIL.COM  
WEIBIN.WYTHE@GMAIL.COM  
WUWJ1024@GMAIL.COM

## Abstract

Due to the lack of depth information of images and poor detection accuracy in monocular 3D object detection, we proposed the instance depth for multi-scale monocular 3D object detection method. Firstly, to enhance the model’s processing ability for different scale targets, a multi-scale perception module based on dilated convolution is designed, and the depth features containing multi-scale information are re-refined from both spatial and channel directions considering the inconsistency between feature maps of different scales. Firstly, we designed a multi-scale perception module based on dilated convolution to enhance the model’s processing ability for different scale targets. The depth features containing multi-scale information are re-refined from spatial and channel directions considering the inconsistency between feature maps of different scales. Secondly, so as to make the model obtain better 3D perception, this paper proposed to use the instance depth information as an auxiliary learning task to enhance the spatial depth feature of the 3D target and use the sparse instance depth to supervise the auxiliary task. Finally, by verifying the proposed algorithm on the KITTI test set and evaluation set, the experimental results show that compared with the baseline method, the proposed method improves by 5.27% in AP40 in the car category, effectively improving the detection performance of the monocular 3D object detection algorithm.

**Keywords:** monocular 3D object detection, instance depth estimation, multi-scale, attention mechanism, auxiliary learning

## 1. Introduction

3D object detection is vital in various computer vision applications, such as autonomous driving (Larson and Trivedi (2011); Imad et al. (2021)), uncrewed aircraft, automatic operation, and augmented reality. 3D detection of targets from monocular images is more complex than 3D target detection using lidar information (Lu et al. (2020)) and multi-camera systems due to the lack of directly calculable target depth information in the image. However, if monocular 3D object detection can achieve reliable detection performance, it will have the advantages of low cost, low power consumption, and flexible deployment in practical applications.

In order to solve the problem of lack of depth information in monocular images, PatchNet (Ma et al. (2020)) and DDMP-3D (Liu et al. (2021b)) adopt the way of adding additional data, that is, using a convolutional neural network regression depth estimation map. However, depth estimation helps 3D object detection, but the existing monocular depth estimation algorithm has limited capabilities, resulting in inaccurate depth estimation and low detection accuracy. Second, inference for such methods could be faster due to additional depth estimation modules. In addition, recent methods introduce efficient but complex geometric prior methods in the network. MonoPair (Chen et al. (2020)) designs an additional pairwise constraint branch that computes the uncertainty perception prediction of object position prediction and 3D distance of adjacent object pairs, followed by joint optimization by the nonlinear least squares method. MonoFlex (Zhang et al. (2021)) proposes a new detector to jointly calculate object position and spatial constraints between pairs of matching objects, which are modeled as critical points at the center of geometry between two adjacent objects, effectively encoding all necessary geometric information to capture the geometric context between objects. GUPNet (Lu et al. (2021)) proposes a geometric uncertainty projection network with a geometric uncertainty projection module and hierarchical task learning strategy to solve the error amplification problem in the projection process. These methods use geometric constraints to compensate for images' lack of accurate depth information. MonoDLE (Ma et al. (2021)) found that positioning error is the reason limiting the performance of monocular 3D detection and proposed three strategies for direct detection of the projected 3D center, discarding distant object samples, and 3DIoU loss, which is a network model built based on CenterNet (Zhou et al. (2019)), and only using local features around the center of the predicted object is not enough to solve scene-level geometric clues to estimate the depth of the object accurately. MonoGRnet (Qin et al. (2021)) breaks down the monocular 3D object detection task into four subtasks, namely 2D object detection, instance-level depth estimation, projected 3D center estimation, and local corner point regression, in which instance-level depth estimation plays an important role in bridging the 2D-to-3D gap. At the same time, in similar 2D object detection work, the model's performance can be effectively improved by adding feature processing at different scales (Ju et al. (2020,?)). YOLOv3-SPP (Zhang et al. (2019)) introduces the spatial pyramid (SPP) (He et al. (2015)) module into YOLOv3 (Redmon and Farhadi (2018)). SPP can extract multi-scale depth features with different receptors and improve the detection accuracy by connecting and fusing in the channel dimension of the feature map, but pooling will cause some information loss. ASPP (Chen et al. (2017)) employs multiple parallel hole convolutional layers with different sampling rates to capture objects and image contexts at multiple scales. For the feature information of different scales, these methods are integrated by splicing and cannot fully utilize the features of different scales.

This article analyzes the above problems based on the MonoDLE method in the KITTI benchmark. First, the depth prediction caused by the lack of depth of the image for monocular 3D target detection needs to be more accurate. 3D perception features acquire the task enhancement model. Secondly, a new multi-scale perception module is designed to enhance the model's ability to obtain different-scale information through this module to improve the detection ability of different scale goals in the image. Finally, the sparse instance depth representation and L1 losses are used to supervise and learn for the depth-assisted learning tasks of the instance. At the same time, the task is only implemented during the training

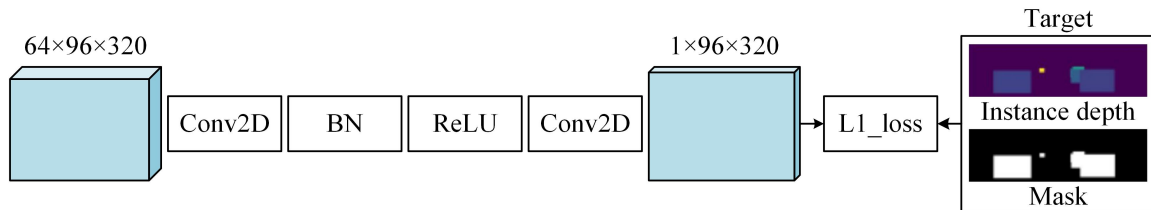


Figure 1: Instance Depth Learning Module

phase and discarded during the reasoning stage. By analyzing the experimental results of the KITTI dataset, the method mentioned in this article is better than the baseline method, and it is competitive compared to the advanced monocular 3D object detection method.

## 2. Method

### 2.1 Instance Depth Learning Module

Monocular 3D object detection degrades performance due to the lack of accurate depth information, and detection accuracy is affected by depth uncertainty. In order to aggregate the global visual features of the object as a hint for depth estimation and improve the accuracy of 3D positioning, instance deep learning module (IDLm) is designed to generate the depth information features of foreground objects, as an auxiliary learning task, by exploring the sizeable sensory field in the feature map to capture the rough instance depth. The auxiliary network learns to better 3D feature representation.

The structure diagram of the example deep learning module is shown in Fig. 1. The module’s input feature map is the feature map  $F \in R^{64 \times 96 \times 320}$  after DLAUP upsampling, and then a  $3 \times 3$  convolution and a  $1 \times 1$  convolution are applied to obtain the instance depth map feature  $F_d \in R^{1 \times 96 \times 320}$  of the input image. In order to enable the network to obtain the rough depth map feature  $F_d$  of the target in the image, it is supervised by the object depth label in the input image, and the 2D bounding box label of the object is used to generate the sample depth map label and mask with a resolution of  $96 \times 320$ . The pixel value in the instance depth map label is assigned by the depth label value of the object in the image. If the enclosure frame between each object has a heavy coincidence, the pixel value of the coincidence is The visual appearance of the image. Secondly, assign the background depth value to 0. The pixel value of the mask is composed of 0 and 1, and the 2D siege of the object in the image generates it. The pixel value in the enclosure box is assigned to 1. Otherwise, it is 0. The pixel-level depth of pixel fixation is not used to reduce the labeling cost, but the depth of the 2D boundary box is directly predated by sparse supervision.

For the generated instance depth map feature  $F_d$ , it is constrained to learn using the L1 loss function, and the expression of the instance depth learning module is:

$$F' = Con(ReLu(BN(Con(F)))) \quad (1)$$

Where  $Con$  stands for two-dimensional convolution,  $ReLu$  represents the Relu activation function,  $BN$  represents the BN layer.

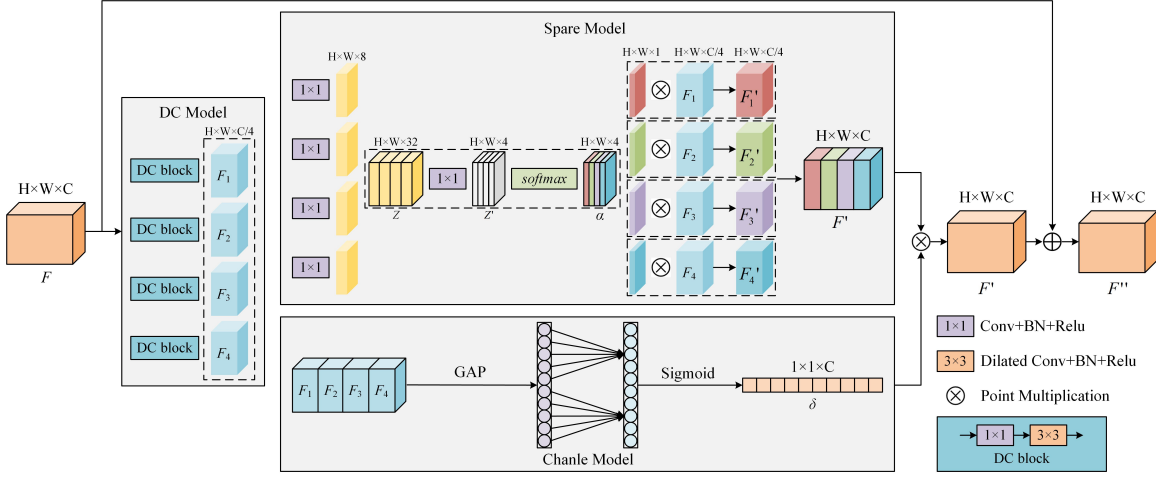


Figure 2: Multi-scale perception module

## 2.2 Multi-scale Perception module

Objects that are close occupy more pixels in the image, far away occupy fewer pixels, and objects with fewer pixels carry less object information. For targets of different scales, different receptive fields are used to obtain the feature map information of the target, which can effectively improve the three-dimensional information acquisition of the target. Therefore, this paper proposes a Multi-Sale perception module (MSP) to learn the feature information of targets at different scales adaptively. The multi-scale perception module consists of a dilated convolution module, a spatial perception module, a channel perception module, and a residual structure. The dilated convolution module is responsible for extracting the feature map information of different receptive fields, the spatial perception module and the channel perception module are responsible for learning the correlation between the feature maps of different receptive fields from the two dimensions of space and channel, respectively, and the residual structure is responsible for weakening the checkerboard effect brought by dilated convolution.

The structure of the multi-scale perception module is shown in Fig. 2. The input feature map of this module is the deep feature map  $F \in R^{H \times W \times C}$  output of the level 5 layer of the DLA34. The dilated convolution module comprises four groups of  $1 \times 1$  standard convolution blocks, and one  $3 \times 3$  dilated convolution block in parallel. Firstly, feature map  $F$  obtains the  $F_1, F_2, F_3$ , and  $F_4$  of different receptive fields through the dilated convolution module. The feature maps of different sizes of receptive fields are obtained by setting the rate in the dilated convolution block. Secondly, for the feature map  $F_1, F_2, F_3$ , and  $F_4$  to input the spatial perception module and the channel perception module to learn the fusion weight, the spatial perception module first uses  $1 \times 1$  standard convolution to reduce the channel dimension of the feature map  $F_1, F_2, F_3$ , and  $F_4$ , then uses the  $1 \times 1$  standard convolution to resample after stitching to obtain the feature  $Z' \in R^{W \times H \times 4}$ . Then, the feature map  $Z'$  is input into the  $\text{SoftMax}$  activation function to obtain weight  $\alpha \in R^{H \times W \times 4}$ ,  $\alpha$  is sliced in the channel dimension to obtain  $\alpha_1 \in R^{H \times W \times 1}, \alpha_2 \in R^{H \times W \times 1}, \alpha_3 \in R^{H \times W \times 1}, \alpha_4 \in R^{H \times W \times 1}$  and then multiplied with feature maps  $F_1, F_2, F_3$ , and  $F_4$  to obtain new

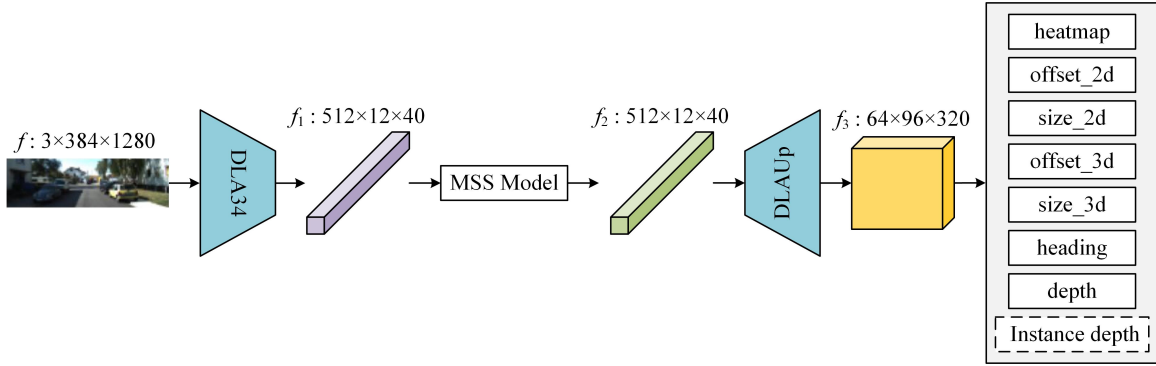


Figure 3: Network structural diagram

feature maps and then fused to stitch the output feature map  $F' \in R^{H \times W \times C}$ . The spatial perception module is expressed as:

$$F' = \text{cat}(\alpha_1 \bullet F_1, \alpha_2 \bullet F_2, \alpha_3 \bullet F_3, \alpha_4 \bullet F_4) \quad (2)$$

Where  $\text{cat}()$  represents the concatenate activation function,  $\bullet$  means bitwise multiplication.

The channel perception module first splices and fuses the feature maps  $F_1$ ,  $F_2$ ,  $F_3$ , and  $F_4$ , then uses the global average pooling GAP to generate global context information, avoids channel data dimensionality reduction through one-dimensional convolution and captures cross-dimensional connections, and outputs channel perception attention feature map  $\delta \in 1 \times 1 \times C$  with the *Sigmoid* activation function.

$$\delta = \text{Sigmoid}(C1D_k(\text{GAP}(\text{cat}(F_1, F_2, F_3, F_4)))) \quad (3)$$

The channel perception module is as above, and *Sigmoid* represents the Sigmoid activation function;  $\text{cat}()$  stands for concatenating.

The channel perception attention feature map  $\delta \times F'$  and the feature map fusion weights of different receptive fields are optimized using global context information to get the feature map  $F'' \in R^{W \times H \times C}$ . In order to weaken the checkerboard effect brought by dilated convolution, the original input deep features map  $F$  and the feature map  $F''$  containing different receptive fields are added to the output feature  $F''' \in R^{W \times H \times C}$  using the residual structure. The calculation of the multi-scale perception module is as follows:

$$F''' = F + \delta + F' \quad (4)$$

### 2.3 Model Architectures

The network architectures is shown in Fig. 3, and the improved monocular 3D object detection method based on MonoDLE proposed in this paper is simple in design and consists of four parts:

- **Backbone feature extraction network.** Given an input image  $f$  with a resolution of  $3 \times 384 \times 1280$ , use a DLA (Yu et al. (2018)) network (DLA34) as the backbone feature extraction network to compute an output feature map  $f_1$  with a dimension of  $512 \times 12 \times 40$ .

- **Multi-scale perception module.** Different from the previous work, for 3D object detection, in order to obtain the feature information of different receptive fields, for the feature map  $f_1$ , this paper uses a multi-scale perception module to resample it to obtain a feature map  $f_2$  with a size of  $512 \times 12 \times 40$ , so that Deep features contain richer multi-scale information.
- **Bounding box regression head.** The heatmap regression head predicts the coarse center using the projected 3D center as the truth value for estimating the coarse center C. The 2D offset branch predicts the offset between the coarse center and the true center of the 2D bounding box. The 2D dimension branch predicts the size of the 2D edge bounding box. The 3D offset branch predicts the offset between the coarse center and the center of the projected 3D bounding box. The 3D Dimensions branch predicts the size of the 3D bounding box. The depth branch predicts the true depth of the target. The angle branch predicts the viewing angle of the target. The last branch of the new design of this paper, the instance depth branch, is responsible for predicting the global depth of the instance, which is only used in the training phase and discarded in the inference phase. In this way, instance deep learning as an auxiliary task helps to learn better 3D perception features.
- **Calculate 3D bounding box.** In the inference phase, each target’s 2D bounding box center is indexed at the peak of the heat map after maximum pooling and threshold (0.2). The predicted 2D and 3D offset, 2D and 3D bounding box size, depth, and viewing angle are indexed, and then the 3D center point of the target and the bounding box position is determined.

## 2.4 Loss function

The loss function of MonoDLE consists of heat map loss function  $L_k$ , 2D offset loss function  $L_{o,2d}$ , 2D size loss function  $L_{s,2d}$ , 3D offset loss function  $L_{o,3d}$ , 3D size loss function  $L_{s,3d}$ , observation angle loss function  $L_{head}$ , and depth loss function  $L_d$ . Unlike MonoDLE, this paper adds an instance depth loss function  $L_{I,d}$  composed of L1 loss functions, and the total loss function is expressed as:

$$L_{total} = L_k + L_{o,2d} + L_{s,2d} + L_{o,3d} + L_{s,3d} + L_{head} + L_d + L_{I,d} \quad (5)$$

The heat map loss function  $L_k$  uses the Focal loss function to solve the problem of sample imbalance, and the calculation is shown in Eq. (6):

$$L_k = \frac{-1}{N} \sum_{xyc} \begin{cases} (1 - \hat{Y}_{xyc})^\alpha \log(\hat{Y}_{xyc}) & \text{if } Y_{xyc} = 1 \\ (1 - Y_{xyc})^\beta (\hat{Y}_{xyc})^\alpha \log(1 - \hat{Y}_{xyc}) & \text{othersize} \end{cases} \quad (6)$$

$\hat{Y}_{xyc}$  is represented as the heat map predicted by the model,  $Y_{xyc}$  is represented as the label value of the heat map,  $\alpha$  and  $\beta$  are hyperparameters, and in this article  $\alpha = 2$ ,  $\beta = 4$ ,  $N$  is the number of objects in the image.

The 2D offset loss function  $L_{o,2d}$ , the 2D dimension loss function  $L_{s,2d}$ , and the 3D offset loss function  $L_{o,3d}$  all use the L1 loss function, which constrains the model’s predictions, as shown in Eq. (6) (7) (9):

$$L_{o,2d} = L_1(S_{o,2d}, S_{o,2d}^*) \quad (7)$$

$$L_{s\_2d} = L_1(S_{s\_2d}, S_{s\_2d}^*) \quad (8)$$

$$L_{o\_3d} = L_1(S_{o\_3d}, S_{o\_3d}^*) \quad (9)$$

$S_{o\_2d}$  represents the predicted 2D offset,  $S_{o\_2d}^*$  represents the GT of the 2D offset,  $S_{s\_2d}$  represents the 2D box size predicted by the model,  $S_{s\_2d}^*$  represents the GT of the 2D box size,  $S_{o\_3d}$  represents the predicted 3D offset,  $S_{o\_3d}^*$  represents the GT of the 3D offset, and  $L_1()$  represents the L1 loss function.

The 3D dimension loss function  $L_{s\_3d}$  uses the dimension perception L1 loss function, as shown in Eq. (10):

$$L_{s\_3d} = L_1 \left| \frac{(S_{s\_3d} - S_{s\_3d}^*)}{S_{s\_3d}} \right| \quad (10)$$

where  $S_{s\_3d}$  represents the 3D box size predicted by the model,  $S_{s\_3d}^*$  represents the GT of the 3D box size and  $L_1()$  represents the L1 loss function.

The depth loss function  $L_d$  adopts the Laplace arbitrary uncertainty loss function,  $d$  represents the target depth value predicted by the model,  $d^*$  represents the label value of the target depth,  $dm$  represents the heteroscedasticity arbitrary uncertainty in depth estimation, and  $L_l()$  represents the Laplace arbitrary uncertainty loss function.

$$L_d = L_l(d, d^*, dm) \quad (11)$$

Observation of the angular loss function  $L_{head}$  uses the standard cross-entropy loss function,  $S_{head}$  represents the observation angle value predicted by the model,  $S_{head}^*$  indicates the observation angle label value of the target,  $L_{cross\_entropy}()$  represents the standard cross-entropy loss function, and as shown in Eq. (12):

$$L_{head} = L_{cross\_entropy}(S_{head}, S_{head}^*) \quad (12)$$

The instance depth loss function  $L_{I\_d}$  adopts the L1 loss function,  $I_d$  represents the instance depth value predicted by the model,  $mask$  represents the mask,  $I_d^*$  represents the instance depth label value, and  $L_1()$  represents the L1 loss function.

$$L_{I\_d} = L_1(I_d * mask, I_d^*) \quad (13)$$

### 3. Experiments

#### 3.1 Datasets

This paper evaluates the effectiveness of the proposed method on the KITTI dataset (Geiger et al. (2013, 2012)), which provides 7481 images for training and 7518 images for testing. Due to the lack of labels for the test set and limited access to submit to the official server for testing, we follow the protocol (Caesar et al. (2020); Chen et al. (2015)) of the previous work to divide the training dataset into a training set (3712 images) and a validation set (3769 images). This paper was studied and analyzed based on this split and finally trained on 7481 images and tested by the official KITTI server.

Method	Extra data	$AP_{3D R40 IoU\geq 0.7}$			$AP_{BEV R40 IoU\geq 0.7}$		
		Easy	Moderate	Hard	Easy	Moderate	Hard
AM3D (Ma et al. (2019))	Depth	16.50	10.74	9.52	25.03	17.32	14.91
PatchNet (Ma et al. (2020))	Depth	15.68	11.12	10.17	22.97	16.86	14.97
DDMP-3D (Liu et al. (2021b))	Depth	19.71	12.78	9.80	28.08	17.89	13.44
(Liu et al. (2022a))	Depth	20.28	13.12	9.56	-	-	-
Kinematic3D (Brazil et al. (2020))	Multi-frames	19.07	12.72	9.17	26.69	17.52	13.10
CaDDN (Reading et al. (2021))	LiDAR	19.17	13.41	11.46	27.94	18.91	17.19
MonoRUn (Chen et al. (2021))	LiDAR	19.65	12.30	10.58	27.94	17.34	15.24
MonoGRNet (Qin et al. (2021))	None	9.61	5.74	4.25	18.19	11.17	8.73
MonoDIS (Simonelli et al. (2019))	None	10.37	7.94	6.40	17.23	13.19	11.12
(Zhou et al. (2022))	None	20.89	14.49	12.19	29.57	20.77	17.88
MonoPair (Chen et al. (2020))	None	13.04	9.99	8.65	19.28	14.83	12.89
FADNet (Gao et al. (2022))	None	16.37	9.92	8.05	23.00	14.22	12.56
MonoDLE (Ma et al. (2021))	None	17.23	12.26	10.29	24.79	18.89	16.00
M3DGAF (Chen et al. (2022))	None	19.48	12.66	10.99	31.34	21.39	13.08
MonoFlex (Zhang et al. (2021))	None	19.94	13.89	12.07	28.23	19.75	16.89
MonoEF (Zhou et al. (2021))	None	21.29	13.87	11.71	29.03	19.70	17.26
(Liu et al. (2021a))	None	21.65	13.25	9.91	29.81	17.98	13.08
GUPNet (Lu et al. (2021))	None	22.26	15.02	13.12	30.29	21.19	18.20
MonoCon (Liu et al. (2022b))	None	22.50	<b>16.49</b>	<b>13.95</b>	31.12	22.10	19.00
Ours	None	<b>22.50</b>	16.19	13.49	<b>32.44</b>	<b>22.97</b>	<b>19.82</b>
Improvement	v.s. Depth	+2.22	+3.07	+3.32	+4.36	+5.08	+4.85
	v.s. Multi-frames	+3.43	+3.47	+4.78	+5.75	+5.45	+6.72
	v.s. LiDAR	+2.85	+2.78	+2.03	+4.5	+4.06	+2.63
	v.s. None	+0	-0.3	-0.46	+1.32	+0.87	+0.82

Table 1: Performance of the Car category on the KITTI test set

The KITTI dataset provides many widely used evaluation metrics for auto-keying scenarios, including 3D detection, bird’s eye view (BEV), and average orientation similarity (AOS). This paper reports the average accuracy of 40 recall positions (AP40) (Simonelli et al. (2019)) for these tasks at three difficulty settings (easy, medium, and hard). This paper mainly tests the performance of the car category, and the default IoU thresholds are 0.7, 0.5, and 0.5.

### 3.2 Experimental setup

The operating system used in the experiment is Linux, the GPU is two RTX 2080Ti, the processor is 24-core Intel(R) Xeon(R) Platinum 8255C CPU @2.50GHz, and the deep learning framework is Pytorch 1.1.0. This paper trains the network end-to-end on 140 epochs and sets the batchsize to 16 while using the Adam optimizer with an initial learning rate of 1.25e-3 and attenuating it by a factor of 90 at 120 epochs. The weight decay is set to 1e-5, and the first 5 epochs use a warm-up strategy. To avoid overfitting, we employ random cropping/scaling (for 2D detection only) and random horizontal flipping. With this setup, the entire training process takes about 9 hours.

Method	$3D@IOU = 0.7$			$BEV@IOU = 0.7$			$3D@IOU = 0.5$			$BEV@IOU = 0.5$			Runtime
	Easy	Mod.	Hard	Easy	Mod.	Hard	Easy	Mod.	Hard	Easy	Mod.	Hard	
CenterNet (Zhou et al. (2019))	0.60	0.66	0.77	3.46	3.31	3.21	20.00	17.50	15.57	34.36	27.91	24.65	-
MonoGRNet	11.90	7.56	5.76	19.72	12.81	10.15	47.59	32.28	25.50	48.53	35.94	28.59	60ms
MonoDIS	11.06	7.60	6.37	18.45	12.58	10.66	-	-	-	-	-	-	-
M3D-RPN	14.53	11.07	8.65	20.85	15.62	11.88	48.53	35.94	28.59	53.35	39.60	31.76	161ms
MonoPair	16.28	12.30	10.42	24.12	18.17	15.76	55.38	42.39	37.99	61.06	47.63	41.92	57ms
MonoDLE	17.45	13.66	11.68	24.97	19.33	17.01	55.41	43.42	37.81	60.73	46.87	41.89	40ms
Ours	<b>22.59</b>	<b>17.79</b>	<b>14.99</b>	<b>30.22</b>	<b>23.31</b>	<b>20.04</b>	<b>64.22</b>	<b>47.49</b>	<b>42.72</b>	<b>68.47</b>	<b>52.12</b>	<b>46.11</b>	<b>45ms</b>
Improvement	+5.14	+4.13	+3.31	+5.25	+3.98	+3.03	+8.81	+4.07	+4.73	+7.41	+4.49	+4.19	-

Table 2: Performance of the Car category on the KITTI validation set

### 3.3 Metrics

In order to verify the effectiveness of the algorithm in this paper, this paper compares with other proposed methods on the KITTI test set, as shown in Table 1. Overall, the algorithm proposed in this paper achieves better results than other classical algorithms. For example, the method proposed in this paper has been improved by 5.27/3.93/3.2 at the easy/moderate/hard settings for the 3D inspection task, respectively. Compared with methods with additional data, such as DDMP-3D and PatchNet, the proposed method still has some competitiveness, which further proves the effectiveness of the proposed method. Secondly, compared with the method without additional data, the performance of the proposed method is higher than that of MonoCon under the BEV task, while the detection ability of MonoCon in the 3D task is slightly better. The best results are highlighted in bold in Table 1 and the second digit is highlighted under underline.

Table 2 shows the algorithm’s performance in this article on the KITTI verification set. Since DORN’s (Fu et al. (2018)) training set overlaps with KITTI3D’s validation set, some methods directly use the pre-trained model provided by DORN as their depth estimator, so this article does not compare with these methods. As can be seen from Table 2, this method performs better for both 3D and BEV tasks. Compared with the baseline network MonoDLE, the ability of the proposed algorithm to detect targets under strict conditions (IOU=0.7) is greatly improved, and the easy/moderate/hard settings of the 3D task and BEV task are improved by 5.14/4.13/3.31 and 5.25/3.98/3.03, respectively. Secondly, the ability of the proposed algorithm to detect targets under loose conditions (IOU=0.5) is significantly improved. The baseline network MonoDLE has no apparent advantages over MonoPair in 3D tasks. Its performance is slightly worse under BEV tasks. However, after improvement, the algorithm in this paper improves 8.81/4.07/4.91 compared with the baseline network under the easy/moderate/hard settings of 3D tasks by introducing multi-scale information, and instance, deep assisted learning. The easy/moderate/hard settings are up 7.41/4.49/4.19 compared to MonoPair. Secondly, the proposed model is tested on a single GTX 1080Ti GPU with a batch size of 1 for runtime analysis, which increases the time consumed by one image in the inference phase by 5ms compared to the baseline method.

Table 3 shows the results of adding a multi-scale perception module and depth guidance module to the KITTI verification set for the proposed algorithm, respectively. As can be seen from Table 3, adding a multi-scale perception module and a depth guidance module to the model can improve its accuracy of the model. Firstly, after adding PSP (Zhao et al.

Method	3D			BEV		
	Easy	Mod.	Hard	Easy	Mod.	Hard
baseline	17.45	13.66	11.68	24.97	19.33	17.01
+ASPP	18.04	14.72	12.47	25.60	20.84	18.20
+PSP	18.98	14.73	12.38	25.61	20.75	18.06
+MSS	20.48	15.89	14.06	28.58	22.41	19.46
+IDL	21.76	16.19	14.24	28.71	22.44	19.43
+MSS+IDL	<b>22.59</b>	<b>17.79</b>	<b>14.99</b>	<b>30.22</b>	<b>23.31</b>	<b>20.04</b>
Improvement	+5.14	+4.13	+3.31	+5.25	+3.98	+3.03

Table 3: Adding Performance Comparison of Different Modules on KITTI validation set

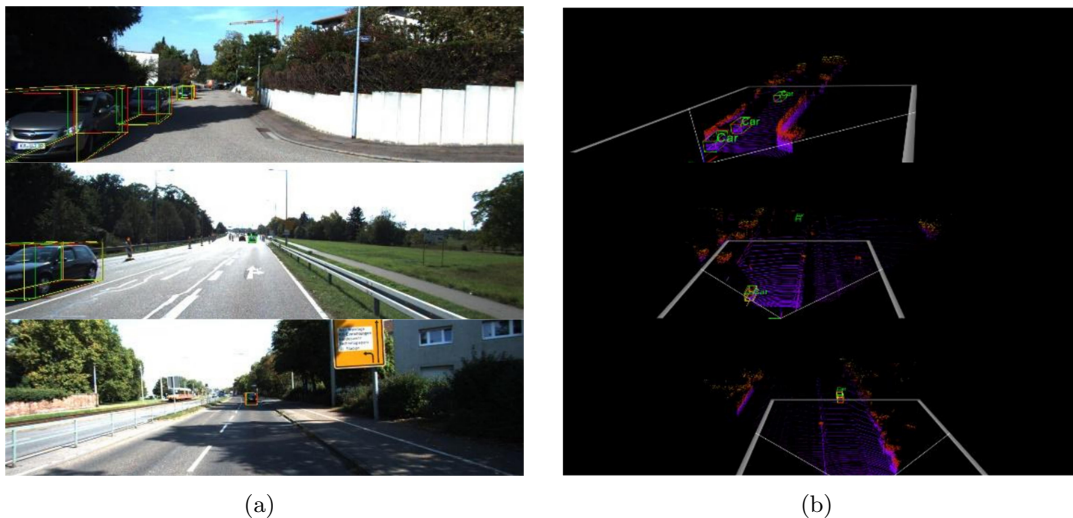


Figure 4: Visualization results of KITTI evaluation set

(2017)) and ASPP structures to the model, the model performance is improved, which shows that introducing a multi-scale information acquisition module in the network can effectively improve the performance of model monocular 3D object detection. Secondly, after adding the multi-scale perception module proposed in this paper, the performance improvement is more evident than that of PSP and ASPP. The detection accuracy under different tasks is improved by fusing the information at different scales from the spatial and channel dimensions and using the residual structure to weaken the checkerboard effect.

In the experiment of adding the instance depth learning modules as an auxiliary task in the training process, to help monocular 3D object detection, let the model learn the instance depth information during the training process so that the model contains more 3D perception features and further improve the positioning accuracy of the model on the target, especially under the simple settings in the 3D task. Finally, in this paper, two modules are applied to the algorithm simultaneously, which enhances the expression ability of the network in the direction of multi-scale information and depth information, thereby improving the model's performance.

### 3.4 Analysis

In order to analyze the effectiveness of the proposed method in this paper, the detection results in the KITTI evaluation set are visualized in Fig. 4. The prediction box of the proposed method, the prediction box of the baseline method, and the truth box are plotted in both the RGB image and the LiDAR signal. The green bounding box, yellow bounding box, and red bounding box in Fig. 4 represent the truth value box, the prediction box of the baseline method, and the prediction box of the method in this paper, respectively. The LiDAR signal is for visualization only, and the target category is labeled in the LiDAR.

By comparing the detection results in the images, it can be found that both the baseline method and the method in this paper output a more accurate 3D bounding box for the target within a reasonable distance. By comparing (b) in Fig. 4, it can be seen that the method proposed in this article outperforms the baseline method in predicting the position, and the prediction box is closer to the truth box. In summary, the method proposed in this paper can effectively improve the performance of monocular 3D object detection models and improve detection accuracy.

## 4. Conclusion

This paper proposes a multi-scale monocular 3D object detection algorithm based on joint instance depth. With the proposed multi-scale perception module for deep features, the multi-scale feature information is obtained by using dilated convolution and re-refining the features from the spatial and channel directions to improve the detection ability of 3D targets at different scales. At the same time, the instance depth-assisted learning task is added, and only the sparse depth label is supervised, which effectively improves the perception ability of the algorithm on 3D features and further improves the perception ability of the algorithm to process 3D objects. Finally, on the KITTI test set, the detection accuracy of the proposed algorithm has been significantly improved, which fully proves the effectiveness of the proposed method. In the next step, the performance will be further improved by exploring the potential of the lidar.

## References

- Garrick Brazil, Gerard Pons-Moll, Xiaoming Liu, and Bernt Schiele. Kinematic 3d object detection in monocular video. In *European Conference on Computer Vision*, pages 135–152. Springer, 2020.
- Holger Caesar, Varun Bankiti, Alex H Lang, Sourabh Vora, Venice Erin Liong, Qiang Xu, Anush Krishnan, Yu Pan, Giancarlo Baldan, and Oscar Beijbom. nuscenes: A multimodal dataset for autonomous driving. In *Proceedings of the IEEE/CVF conference on computer vision and pattern recognition*, pages 11621–11631, 2020.
- Hansheng Chen, Yuyao Huang, Wei Tian, Zhong Gao, and Lu Xiong. Monorun: Monocular 3d object detection by reconstruction and uncertainty propagation. In *Proceedings of the IEEE/CVF Conference on Computer Vision and Pattern Recognition*, pages 10379–10388, 2021.

- Liang-Chieh Chen, George Papandreou, Iasonas Kokkinos, Kevin Murphy, and Alan L Yuille. Deeplab: Semantic image segmentation with deep convolutional nets, atrous convolution, and fully connected crfs. *IEEE transactions on pattern analysis and machine intelligence*, 40(4):834–848, 2017.
- Mu Chen, Pengfei Liu, and Huaici Zhao. M3dgaf: Monocular 3d object detection with geometric appearance awareness and feature fusion. *IEEE Sensors Journal*, 2022.
- Xiaozhi Chen, Kaustav Kundu, Yukun Zhu, Andrew G Berneshawi, Huimin Ma, Sanja Fidler, and Raquel Urtasun. 3d object proposals for accurate object class detection. *Advances in neural information processing systems*, 28, 2015.
- Yongjian Chen, Lei Tai, Kai Sun, and Mingyang Li. Monopair: Monocular 3d object detection using pairwise spatial relationships. In *Proceedings of the IEEE/CVF Conference on Computer Vision and Pattern Recognition*, pages 12093–12102, 2020.
- Huan Fu, Mingming Gong, Chaohui Wang, Kayhan Batmanghelich, and Dacheng Tao. Deep ordinal regression network for monocular depth estimation. In *Proceedings of the IEEE conference on computer vision and pattern recognition*, pages 2002–2011, 2018.
- Tianze Gao, Huihui Pan, and Huijun Gao. Monocular 3d object detection with sequential feature association and depth hint augmentation. *IEEE Transactions on Intelligent Vehicles*, 2022.
- Andreas Geiger, Philip Lenz, and Raquel Urtasun. Are we ready for autonomous driving? the kitti vision benchmark suite. In *2012 IEEE conference on computer vision and pattern recognition*, pages 3354–3361. IEEE, 2012.
- Andreas Geiger, Philip Lenz, Christoph Stiller, and Raquel Urtasun. Vision meets robotics: The kitti dataset. *The International Journal of Robotics Research*, 32(11):1231–1237, 2013.
- Kaiming He, Xiangyu Zhang, Shaoqing Ren, and Jian Sun. Spatial pyramid pooling in deep convolutional networks for visual recognition. *IEEE transactions on pattern analysis and machine intelligence*, 37(9):1904–1916, 2015.
- Muhammad Imad, Oualid Doukhi, and Deok-Jin Lee. Transfer learning based semantic segmentation for 3d object detection from point cloud. *Sensors*, 21(12):3964, 2021.
- MR Ju, JN Luo, ZB Wang, and H Luo. Multi-scale target detection algorithm based on attention mechanism. *Acta Opt. Sin.*, 466:132–140, 2020.
- Jacoby Larson and Mohan Trivedi. Lidar based off-road negative obstacle detection and analysis. In *2011 14th International IEEE Conference on Intelligent Transportation Systems (ITSC)*, pages 192–197. IEEE, 2011.
- He Liu, Huaping Liu, Yikai Wang, Fuchun Sun, and Wenbing Huang. Fine-grained multi-level fusion for anti-occlusion monocular 3d object detection. *IEEE Transactions on Image Processing*, 2022a.

- Xianpeng Liu, Nan Xue, and Tianfu Wu. Learning auxiliary monocular contexts helps monocular 3d object detection. In *Proceedings of the AAAI Conference on Artificial Intelligence*, volume 36, pages 1810–1818, 2022b.
- Yuxuan Liu, Yuan Yixuan, and Ming Liu. Ground-aware monocular 3d object detection for autonomous driving. *IEEE Robotics and Automation Letters*, 6(2):919–926, 2021a.
- Zongdai Liu, Dingfu Zhou, Feixiang Lu, Jin Fang, and Liangjun Zhang. Autoshape: Real-time shape-aware monocular 3d object detection. In *Proceedings of the IEEE/CVF International Conference on Computer Vision*, pages 15641–15650, 2021b.
- Bing Lu, Phuong D Dao, Jiangui Liu, Yuhong He, and Jiali Shang. Recent advances of hyperspectral imaging technology and applications in agriculture. *Remote Sensing*, 12(16):2659, 2020.
- Yan Lu, Xinzhu Ma, Lei Yang, Tianzhu Zhang, Yating Liu, Qi Chu, Junjie Yan, and Wanli Ouyang. Geometry uncertainty projection network for monocular 3d object detection. In *Proceedings of the IEEE/CVF International Conference on Computer Vision*, pages 3111–3121, 2021.
- Xinzhu Ma, Zihui Wang, Haojie Li, Pengbo Zhang, Wanli Ouyang, and Xin Fan. Accurate monocular 3d object detection via color-embedded 3d reconstruction for autonomous driving. In *Proceedings of the IEEE/CVF International Conference on Computer Vision*, pages 6851–6860, 2019.
- Xinzhu Ma, Shinan Liu, Zhiyi Xia, Hongwen Zhang, Xingyu Zeng, and Wanli Ouyang. Rethinking pseudo-lidar representation. In *European Conference on Computer Vision*, pages 311–327. Springer, 2020.
- Xinzhu Ma, Yinmin Zhang, Dan Xu, Dongzhan Zhou, Shuai Yi, Haojie Li, and Wanli Ouyang. Delving into localization errors for monocular 3d object detection. In *Proceedings of the IEEE/CVF Conference on Computer Vision and Pattern Recognition*, pages 4721–4730, 2021.
- Zengyi Qin, Jinglu Wang, and Yan Lu. Monogrnet: A general framework for monocular 3d object detection. *IEEE transactions on pattern analysis and machine intelligence*, 2021.
- Cody Reading, Ali Harakeh, Julia Chae, and Steven L Waslander. Categorical depth distribution network for monocular 3d object detection. In *Proceedings of the IEEE/CVF Conference on Computer Vision and Pattern Recognition*, pages 8555–8564, 2021.
- Joseph Redmon and Ali Farhadi. Yolov3: An incremental improvement. *arXiv preprint arXiv:1804.02767*, 2018.
- Andrea Simonelli, Samuel Rota Bulo, Lorenzo Porzi, Manuel López-Antequera, and Peter Kotschieder. Disentangling monocular 3d object detection. In *Proceedings of the IEEE/CVF International Conference on Computer Vision*, pages 1991–1999, 2019.

- Fisher Yu, Dequan Wang, Evan Shelhamer, and Trevor Darrell. Deep layer aggregation. In *Proceedings of the IEEE conference on computer vision and pattern recognition*, pages 2403–2412, 2018.
- Pengyi Zhang, Yunxin Zhong, and Xiaoqiong Li. Slimyolov3: Narrower, faster and better for real-time uav applications. In *Proceedings of the IEEE/CVF International Conference on Computer Vision Workshops*, pages 0–0, 2019.
- Yunpeng Zhang, Jiwen Lu, and Jie Zhou. Objects are different: Flexible monocular 3d object detection. In *Proceedings of the IEEE/CVF Conference on Computer Vision and Pattern Recognition*, pages 3289–3298, 2021.
- Hengshuang Zhao, Jianping Shi, Xiaojuan Qi, Xiaogang Wang, and Jiaya Jia. Pyramid scene parsing network. In *Proceedings of the IEEE conference on computer vision and pattern recognition*, pages 2881–2890, 2017.
- Dingfu Zhou, Xibin Song, Jin Fang, Yuchao Dai, Hongdong Li, and Liangjun Zhang. Context-aware 3d object detection from a single image in autonomous driving. *IEEE Transactions on Intelligent Transportation Systems*, 2022.
- Xingyi Zhou, Dequan Wang, and Philipp Krähenbühl. Objects as points. *arXiv preprint arXiv:1904.07850*, 2019.
- Yunsong Zhou, Yuan He, Hongzi Zhu, Cheng Wang, Hongyang Li, and Qinhong Jiang. Monoef: Extrinsic parameter free monocular 3d object detection. *IEEE Transactions on Pattern Analysis and Machine Intelligence*, 2021.